Optical material anisotropy in high-index transition metal dichalcogenide Mie nanoresonators

optica

Optical material anisotropy in high-index transition metal dichalcogenide Mie nanoresonators

Thomas D. Green,[1] Denis G. Baranov,[1] Battulga Munkhbat,[1] Ruggero Verre,[1,2] Timur Shegai,[1] and Mikael Käll[1,3]

[1]Department of Physics, Chalmers University of Technology, 412 96 Göteborg, Sweden
[2]e-mail: ruggero.verre@chalmers.se
[3]e-mail: mikael.kall@chalmers.se

Received 28 January 2020; revised 8 May 2020; accepted 8 May 2020 (Doc. ID 389192); published 8 June 2020

Resonant optical antennas provide unprecedented opportunities to control light on length scales far below the diffraction limit. Recent studies have demonstrated that nanostructures made of multilayer transition metal dichalcogenides (TMDCs) can exhibit well-defined and intense Mie resonances in the visible to the near-infrared spectral range. These resonances are realizable because the TMDC materials exhibit very high in-plane refractive indices, in fact higher than what is found in typical high-index dielectric materials like Si or GaAs. However, their out-of-plane refractive indices are comparatively low. Here we experimentally and theoretically investigate how this unusually large material anisotropy influences the optical response of individual TMDC nanoresonators made of MoS_2. We find that anisotropy strongly affects the far-field optical response of the resonators, as well as complex interference effects, such as anapole and resonant Kerker conditions. Moreover, we show that it is possible to utilize the material anisotropy to probe the vectorial nature of the nanoresonator internal near fields. Specifically, we show that Raman spectra originating from individual MoS_2 nanoresonators exhibit mode-specific anisotropic enhancement factors that vary with the nanoresonator size and correlate with specific modes supported at resonance. Our study indicates that exploring material anisotropy in novel high-index dielectrics may lead to new nanophotonic effects and applications.

https://doi.org/10.1364/OPTICA.389192

1. INTRODUCTION

The ability to fabricate nanostructures of a wide variety of shapes, sizes, and compositions has driven the nanophotonics revolution of the last decades. Nanostructuring enables almost arbitrary control of the optical near fields, which can be explored in the context of enhanced light–matter interaction and unconventional light management. While nanophotonics was for a long time completely dominated by metallic (plasmonic) nanostructures, much recent work has been devoted to high-index dielectrics since the geometrical Mie resonances supported by high-index dielectric nanoantennas exhibit significantly reduced light absorption [1]. High-index nanophotonics is thus a rapidly growing field with potential for applications such as functional metasurfaces [2,3], holograms [4], nonlinear light generation [5,6], light harvesting [7,8], and sensing [9–11]. To date, most dielectric nanoresonators have been fabricated from materials such as Si and GaAs with $n \approx 3.5$ in the lossless region [12].

Essentially, all bulk materials considered so far in nanophotonics are either isotropic or only weakly birefringent in the visible to near-infrared wavelength range, with ordinary and extraordinary refractive indices differing by not more than ∼10% [Fig. 1(a)]. Researchers working in this wavelength region therefore seldom had reasons to consider material anisotropy as a useful degree of freedom when designing nanophotonics elements and optical antennas. On the other hand, anisotropy achieved by engineering the effective refractive index though nanostructuring is a well-known inherent property of artificial metamaterials. In this case, the index contrast between different directions makes it possible to create extremely powerful structures that can, for example, tailor the optical wavefront [13], be integrated for optical on-chip communication [14–16], or control polarization beyond what is possible using standard optical elements [17,18]. Optical anisotropy is also prominent in the phonon frequency region of naturally occurring hyperbolic materials such as hexagonal boron nitride, where nanostructuring can be used to generate subwavelength anisotropic localized phonon polariton resonances for infrared wavelengths [19,20].

In contrast to standard materials, group VI semiconductor transition metal dichalcogenides (TMDCs) are layered materials and present an anisotropy ($\Delta = n_e - n_o$)>70% and reaching values exceeding 200% at specific wavelengths, with refractive index higher than Si in the plane of the layers and much lower in the out-of-plane direction [see Fig. 1(a)]. Dichalcogenide materials have been the subject of intense research in recent years due to their unique optical and electronic properties [21]. Most recent research

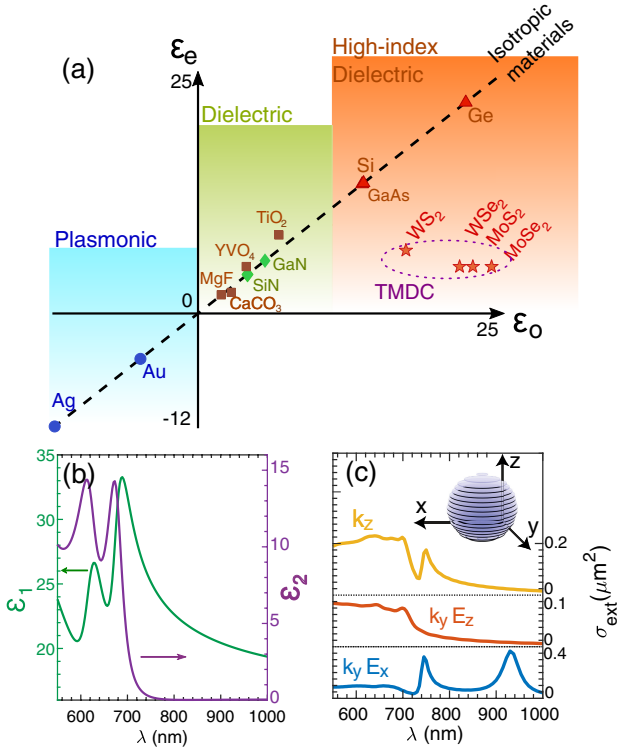

Fig. 1. (a) Real ordinary (ε_o) and extraordinary (ε_e) permittivity of various materials typically used in nanophotonics. Isotropic materials include metals (blue dots, $\lambda = 533$ nm), dielectric materials (green diamonds, $\lambda = 800$ nm), and high-index dielectrics (red triangles, $\lambda = 800$ nm). Birefringent materials (brown squares, $\lambda = 633$ nm) show differences in refractive index within 10% and only moderately high permittivity. Layered TMDC materials show record-high in-plane permittivity and birefringence larger than 70%. (b) Real (solid line) and imaginary (dashed line) components of the in-plane permittivity of 2H-MoS_2. (c) Mie resonances of a MoS_2 nanosphere of radius 100 nm in air. Because of material anisotropy, the scattering spectra and the excited modes sensitively depend on the illumination direction and polarization.

has focused on single-layer TMDCs, since these materials exhibit a direct electronic band gap, [22] which makes them interesting for applications like light harvesting, [23–26] catalysis [27–29] and spintronics, [30,31] as well as for fundamental investigations of strong light–matter interactions [32,33]. Recently, we demonstrated an additional and potentially far-reaching functionality of TMDCs, namely, that nanoparticles made of multilayer WS_2 support Mie resonances due to the large in-plane refractive index of the material [34].

In this work, we investigate how material anisotropy influences the optical response of Mie nanoresonators made of TMDC materials. We show that material anisotropy can be used to influence the far-field response of the Mie modes supported by a nanoresonator and that it can be used as a platform for studying new nanophotonic phenomena. Specifically, we used the anisotropic Raman scattering from single MoS_2 nanoparticles to retrieve information on the vectorial nature and relative strength of the nanoresonators' internal near fields. This is possible because TMDCs support distinct Raman-active optical phonons polarized both in the plane of the layers and out of plane according to the symmetry of the specific modes. Thus, the in-plane and out-of-plane phonon modes are selectively enhanced depending on the orientation and strength of the induced local fields. Additionally, the material anisotropy also influences the far-field response of the complex Mie modes supported by a nanoresonator. These results are, to the best of our knowledge, the first demonstration of how material anisotropy can be used as a new degree of freedom within the context of all-dielectric nanophotonics.

2. MATERIAL OPTICAL ANISOTROPY IN MoS_2

Because of its low loss in the NIR and the very high birefringence [see Fig. 1(a)], we primarily focus on MoS_2 to demonstrate the effects of material anisotropy. The complex in-plane permittivity $\varepsilon_{xy} = \varepsilon_{1xy} + i\varepsilon_{2xy}$ of bulk MoS_2 is presented in Fig. 1(b) [35]. The material exhibits a very high in-plane refractive index ($n_{xy} = \mathrm{Re}(\sqrt{\varepsilon_{xy}}) > 4$) and low absorption ($\varepsilon_{2xy} \approx 0.01$) in the NIR region and strong excitonic absorption bands at shorter wavelengths. Despite the interest in TMDC materials and extensive studies during the 1970s, [36] the out-of-plane refractive index is a much less explored quantity [37,38]. In the following, we use the in-plane value from Fig. 1(b) and $\varepsilon_z = 4.9$ reported for 2H-MoS2 in Ref. [34], while noting that there is considerable uncertainty regarding the out-of-plane value [39].

We first investigated how the highly anisotropic permittivity influences the optical response of a spherical nanoresonator, where shape anisotropy (shape birefringence) cannot occur [Fig. 1(c)]. We simulated scattering cross-section spectra for a 100 nm radius nanosphere in air for the three principal incident wavevector-polarization configurations. All spectra exhibit pronounced resonance peaks, but the peak positions, widths, and intensities vary greatly depending on how the nanosphere is excited, despite the spherical geometry. To reveal the nature of the spectral features, we tracked the resonance positions as a function of sphere radius (Fig. S1, Supplement 1). The results show that the resonances disperse linearly with size above ~700 nm, where material dispersion $\varepsilon(\lambda)$ and absorption is relatively weak. This is the expected behavior for geometrical Mie resonances in high-index nanostructures. We also performed multipolar decomposition of the induced polarization inside the nanosphere as a function of illumination conditions (see Fig. S2 and Methods, Supplement 1 for details). This analysis indicates that in-plane polarized incidence excites electric-dipole-like and magnetic-dipole-like modes of the sphere, whereas out-of-plane polarized light only excites a magnetic resonance because of the longer effective wavelength perpendicular to the MoS_2 planes.

3. SAMPLE FABRICATION AND OPTICAL CHARACTERIZATION

The theoretical results above clearly demonstrate that material anisotropy can profoundly influence the optical properties of a nanoresonator. Unfortunately, spherical TMDC nanoantennas are currently impossible to realize in practice. In the following we therefore focus on in-plane circularly symmetric nanoparticles. The deviation from spherical symmetry implies that any anisotropic response of the structures will in principle be due to a combination of material and shape anisotropy. We start by fabricating particles of varying diameter from transferred MoS_2 flakes by a combination of electron-beam lithography and dry etching (see Supplement 1 for details). In Fig. S3 of Supplement 1, we show that it is possible to apply the same method to fabricate TMDC nanoparticles of MoS_2, $MoSe_2$, WS_2, and WSe_2. The resulting

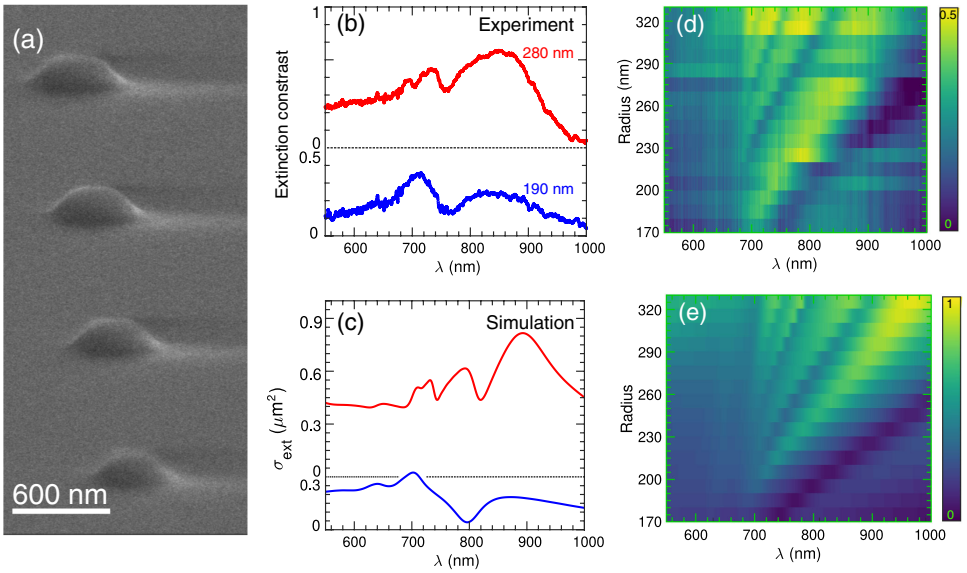

Fig. 2. MoS_2 nanostructures support Mie resonances in the visible and near-infrared wavelength range due a high in-plane refractive index. (a) SEM images of the fabricated MoS_2 nanoresonators. (b) Measured extinction contrast spectra and (c) simulated extinction cross-section spectra of MoS_2 nanocones, showing the presence of Mie resonances. (d) Experimental and (e) simulated extinction cross section in μm^2 of MoS_2 nanocones versus base radius and wavelength demonstrating a linear mode dispersion in the near-infrared.

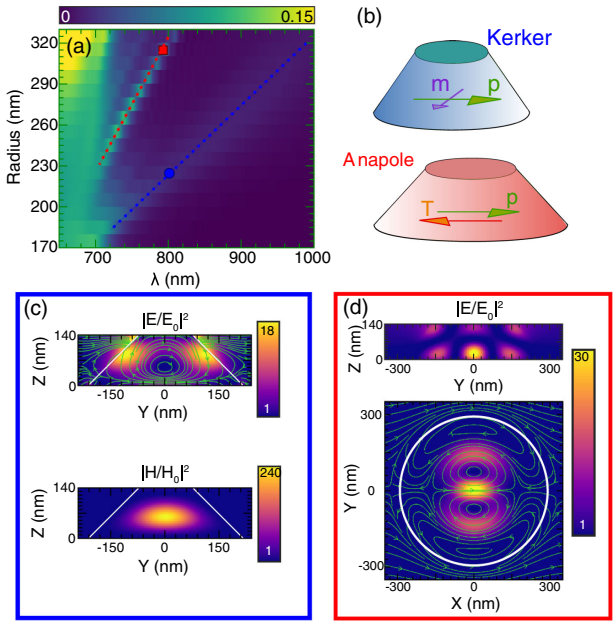

Fig. 3. MoS_2 nanoresonators support multiple resonant modes with complex near-field profiles. (a) Simulated absorption cross-section spectra in μm^2 of MoS_2 nanocones as a function of base radius. (b) Sketch of the modes responsible for anapole and Kerker interference effects. (c) Electric and magnetic field distributions for a 230 nm radius nanocone at 785 nm indicating the presence of both electric and magnetic modes. (d) Anapole-like out-of-plane and in-plane electric field distributions and field lines for a 300 nm base nanocone at 785 nm.

particles are single crystalline and can be potentially realized on any substrate of choice.

Scanning electron microscope (SEM) images of representative nanostructures are presented in Fig. 2(a). We note that the dry-etch step yields conical nanodisk shapes. This is likely due to carbon that deposits on the particle sidewalls during etching and then acts as a mask material. Interestingly, we found that while Mo-based materials yielded nanostructures with sloping sidewalls, i.e., "nanocones," the W-based samples showed an almost vertical profile (Fig. S3, Supplement 1), confirming a chemical origin of this effect.

Next, we studied the optical properties of individual MoS_2 nanocones as a function of their in-plane dimension [Figs. 2(b)–2(e)]. To this end, we measured transmission T using a 1 μm^2 confocal probe area centered on the particle and normalized the recorded spectrum with the transmission T_0 through an empty glass slide. The measured effective single particle extinction contrast $E = 1 - T/T_0$ is shown in Fig. 2(f) as a function of the base radius of the nanocones. The extinction contrast exceeds 0.5 for the largest particles at resonance, indicating a large optical cross section. As expected for high-index dielectric nanostructures, the nanocones exhibit prominent resonant features that disperse linearly with the size in the NIR region, where both material dispersion $\delta n/\delta\lambda$ and absorption are low. Simulated extinction spectra of MoS_2 nanocones with the same size and tapering angle [Figs. 2(c) and 2(e)] are in good overall agreement with the experimental data despite the complex shape of the nanostructures. The excitonic absorption bands at ~620 and ~680 nm [Fig. 1(b)] induce strong bending of the Mie resonance dispersion with radius in the visible wavelength range. This effect, which also occurs for WS_2 nanodisks, is caused by hybridization between the geometrical modes and the excitons, resulting in an avoided crossing [26]. However, the coupling is less pronounced in the MoS_2 case, possibly due to a smaller exciton oscillator strength and higher dissipation compared to WS_2 [31].

In the NIR, where the material in-plane absorption is low, the TMDC Mie nanoresonators can be used as a low-loss nanophotonics platform similarly to isotropic all-dielectric nanoresonators. In Fig. 3(a), we show simulated absorption cross-section spectra of MoS_2 nanocones. The data reveals two absorption features

that disperse linearly with size as indicated by the dashed lines. Note that, due to the relatively large in-plane sizes of the MoS_2 nanoparticles, elastic scattering dominates over absorption, which contribute less than ∼10% to the overall extinction. Thus, scattering interferences between the resonances, indicated in Fig. 3(b), play a crucial role in determining the shape and amplitudes of the extinction spectra shown in Fig. 2.

In the following, we analyze the two absorption features at the laser excitation wavelength 785 nm used in the Raman experiments discussed in the next section. The first absorption peak crosses 785 nm at ∼230 nm radius [blue dot in Fig. 3(a)]. Plots of the corresponding electric and magnetic intensity enhancement factors in a vertical cut in the $y-z$ plane reveals circulating currents indicative of a magnetic Mie resonance [Fig. 3(c)]. To identify the multipoles contributing to this field pattern, we decompose the induced polarization into Cartesian multipoles (Fig. S4, see Supplement 1). The analysis reveals that the 230 nm radius nanocone exhibits both resonant electric (p) and magnetic (m) dipole moments with comparable magnitudes and vanishing phase difference. This situation corresponds to the first Kerker condition, characterized by a large forward-to-backward (F/B) scattering ratio [40–42]. In fact, the data indicates that is possible to reach F/B ratios of 50–100 for specific particle radii and wavelengths. Experimental reflection measurements (Fig. S5, Supplement 1) indicate that the MoS_2 nanostructures indeed enter a regime of reduced backscattering, but a detailed experimental quantification of this effect goes beyond the scope of this work.

The second absorption peak crosses 785 nm at a radius of ∼300 nm [red dot in Fig. 3(a)]. The corresponding near-field distribution [Fig. 3(c)] in the $x-y$ plane resembles a so-called anapole—an interference effect characterized by enhanced internal fields and suppressed far-field scattering [43]. This phenomenon is due to destructive interference of the far fields generated by electric dipole p and toroidal electric dipole T moments in the particle. Indeed, we observe suppression of extinction, which is dominated by scattering, in experiment and simulations around 785 nm, but also an enhancement of internal in-plane near fields.

Similarly to the case of the sphere [Fig. 1(c)], one would like to pinpoint how material anisotropy influences the far-field properties for the fabricated MoS_2 nanoresonators. To this end we performed polarization-dependent dark-field scattering measurements by illuminating the particles with either p- or s-polarized light at a high oblique angle (see Fig. S6, Supplement 1). The data show complex polarization-dependent scattering, but a detailed analysis is difficult due to the low symmetry of the nanostructure and the off-axis illumination condition.

4. RAMAN ENHANCEMENT IN MoS_2 NANORESONATORS

We have thus far analyzed the far-field response of Mie resonators made of anisotropic materials. These resonators act as optical cavities that enhance internal electromagnetic fields at specific resonance wavelengths. This allows for enhancement of various optical processes originating from within the particle, such as nonlinear frequency conversion [5], fluorescence, [44], and Raman scattering [45]. Here we focus on Raman scattering, since the presence of Raman-active phonon modes with well-defined displacement patterns can be correlated with material anisotropy. A typical Raman spectrum obtained in backscattering geometry from the basal plane of a bulk MoS_2 crystal using nonresonant 785 nm laser excitation is shown in the top panel of Fig. 4(a) (see Methods in Supplement 1). There are two peaks in the frequency range investigated. These peaks, centered at 385 cm^{-1} and 410 cm^{-1}, are due to the E^1_{2g}- and A_{1g}-symmetry optical phonon modes with vibration displacements within and perpendicular to the MoS_2 planes, respectively [see Fig. 4(b)].

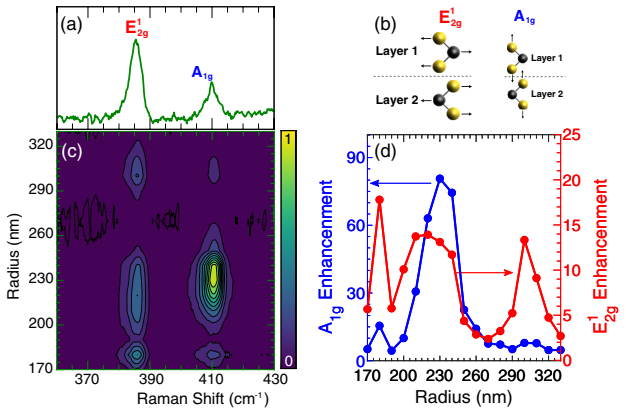

Fig. 4. Raman spectrum of bulk crystalline MoS_2 is enhanced and modified in Mie resonators. (a) Typical unpolarized Raman spectrum of bulk MoS_2 obtained in backscattering geometry for incidence normal to the basal plane and nonresonant excitation at 785 nm. (b) Sketch of the atomic vibration related to the two Raman modes. (c) Single-particle Raman spectra of MoS_2 nanoresonators, demonstrating enhancement of the scattering signal at specific particle sizes. (d) Volume-averaged Raman intensity of the $\mathbf{A_{1g}}$ (blue) and $\mathbf{E^1_{2g}}$ (red) modes measured in single nanocones, relative to the signal obtained from an unpatterned film, as a function of particle bottom radius.

Figure 4(c) shows Raman spectra from single MoS_2 nanoresonators as a function of their base radius. The relative peak intensities, here normalized by the nanoresonator volume, show a nontrivial dependence on the nanodisk size, suggesting that different enhancements originate from the geometrical resonances of the nanoparticles. Remarkably, the relative intensities of the two peaks are inverted at around 230 nm and 300 nm radii. This behavior is also seen in Fig. 4(d), where the volume-averaged Raman intensities of the A_{1g} and E^1_{2g} modes instead have been normalized to the intensities obtained from an unpatterned flake of the same thickness as the nanocones and by assuming a diffraction-limited sampling area. The resulting Raman enhancement factor reaches ∼13 for the E^1_{2g} and ∼80 for the A_{1g} mode, confirming a strong internal field enhancement. Scattering from the A_{1g} mode is clearly enhanced in resonators with base radius of approximately 230 nm, while the E^1_{2g} mode exhibits a distinct enhancement maximum at around 300 nm. These nanocone sizes match the maxima observed in the absorption spectra [Fig. 3(a)] at the Raman excitation wavelength 785 nm. As is well known, absorption scales with the electric field intensity inside the nanostructure and the imaginary component of the material's permittivity as a multiplying factor. As the permittivity tensor is isotropic within the basal plane and real in the perpendicular direction, the absorption cross section reads as $\sigma_{abs} \propto \varepsilon_2(\omega) \int_V (|E_x(\omega_L, r)|^2 + |E_y(\omega_L, r)|^2) d^3r$, where ε_2 is the imaginary part of the in-plane permittivity from Fig. 1(b). The strong modulation of the Raman intensity with the nanostructure size thus reflects the geometric modes of the nanostructure

going into resonance with the excitation and emission frequencies. However, because of the material anisotropy, mode-specific near-field profiles are probed in the Raman scattering process in different ways compared to standard high-index dielectric materials. We note that the additional peak appearing for E^1_{2g} at 180 nm does not correspond to a specific mode [cf. the mode dispersion in Fig. 3(a)], and it is likely caused by overestimated noise in the volume-normalized enhancement at small radii.

To analyze and interpret the obtained results, we need to establish a relationship between the electromagnetic field induced in a single-crystalline resonator and the Raman signal recorded in a particular scattering geometry. For a bulk material, the intensity of Raman scattering from a particular phonon mode σ is proportional to

$$I_{\text{Raman}} \propto \left| \sum_{\sigma} \mathbf{e}_{\text{inc}} \overleftrightarrow{\mathbf{R}}_{\sigma} \mathbf{e}_{\text{scat}} \right|^2, \tag{1}$$

where $\mathbf{e}_{\text{inc}}$ and $\mathbf{e}_{\text{scat}}$ are unit vectors defining the polarization of the incident and scattered photons, respectively, and $\overleftrightarrow{\mathbf{R}}_{\sigma}$ is the Raman polarizability tensor of phonon mode σ. The Raman polarizability is determined by the symmetry of the crystal structure, the vibrational displacement pattern of the phonon mode and the electron-phonon coupling strength [46]. MoS_2 has D_{6h} point symmetry, and the Raman tensors of the E^1_{2g} and A_{1g} modes have the structure [47]

$$\overleftrightarrow{\mathbf{R}}_{E^1_{2g}} = \begin{bmatrix} d & 0 & 0 \\ 0 & -d & 0 \\ 0 & 0 & 0 \end{bmatrix}, \begin{bmatrix} 0 & d & 0 \\ d & 0 & 0 \\ 0 & 0 & 0 \end{bmatrix},$$

$$\overleftrightarrow{\mathbf{R}}_{A_{1g}} = \begin{bmatrix} a & 0 & 0 \\ 0 & a & 0 \\ 0 & 0 & b \end{bmatrix}. \tag{2}$$

The relative strengths of the Raman tensor elements a, b, and d for 785 nm excitation were determined by recording Raman spectra from thick MoS_2 flakes in different scattering geometries A(B,C)D, where A/D indicate the direction of the incident and scattered fields and B/C their polarization. From this analysis (see Supplement 1 and Fig. S7), the relative matrix elements were estimated to $a \approx 0.46$, $b \approx 1.0$, and $d \approx 0.72$.

In order to describe Raman scattering from MoS_2 nanoresonators, we now employ the classical electromagnetic description of Raman scattering [48]. In this framework, the local excitation field at the laser frequency ω_L inside the particle, $\mathbf{E}_{\text{exc}}(\mathbf{r}, \omega_L)$ determines the local induced Raman polarization $\mathbf{P}_S$ oscillating at the Stokes-shifted frequencies. The Stokes Raman polarization is then given by

$$\mathbf{P}_s(\mathbf{r}, \omega_L, \omega_s) = \overleftrightarrow{\mathbf{R}}_{\boldsymbol{\sigma}}(\mathbf{r}, \omega_L, \omega_s)\, \mathbf{E}_{\text{exc}}(\mathbf{r}, \omega_L), \tag{3}$$

where $\omega_S = \omega_L - \Omega$ and Ω is the phonon frequency. The total intensity of the radiated Raman signal can be calculated by integrating the Poynting vector generated by the Raman polarization $\mathbf{P}_S$ over a surface enclosing the entire particle. Generally, this requires knowledge of the Green tensor of the system and consecutive calculation of the radiated electric and magnetic fields. However, we are only interested in the emission radiated in the backscattering direction. Thus, we utilize the electromagnetic reciprocity theorem and instead calculate enhancement factors for the E_v ($v = x, y, z$) field component generated by a normally incident x-polarized plane wave at the Stokes-shifted wavelength. This quantity is a measure of the Raman enhancement in backscattering of a v-polarized point electric dipole oscillating at the Raman emission frequency. We also assume a small Stokes shift compared to the excitation frequency for both the E^1_{2g} and A_{1g} mode (i.e., $\omega_L \sim \omega_S$). This treatment is equivalent to the $|E|^4$ approximation often used in surface-enhanced Raman scattering [49]. Furthermore, we will assume that the Raman polarization is uncorrelated in space; that is, each Raman point dipole inside the particle contributes incoherently to the total Raman intensity. Finally, we will assume that the induced y component of the electric field inside the particle is negligible for x-polarized excitation, which is justified by finite-difference time domain (FDTD) simulations in the following. Under these assumptions, we arrive at the following simple expressions for the Raman intensities emitted by the two independent vibrational modes of the crystal (see Supplement 1):

$$I_{E^1_{2g}} \propto |d|^2 \int_V |E_x(r, \omega_L)|^4 \mathrm{d}^3 r,$$

$$I_{A_{1g}} \propto |a|^2 \int_V |E_x(r, \omega_L)|^4 \mathrm{d}^3 r + |b|^2 \int_V |E_z(r, \omega_L)|^4 \mathrm{d}^3 r. \tag{4}$$

The integration is performed over the interior volume of the nanostructure, and the electric fields represent the induced local fields inside the nanostructure.

Equation (4) implies a direct relation between the Raman intensity and the average vectorial electric field intensity inside the nanoparticle. The relative intensity of the two Raman modes can thus be exploited as an experimental probe of the vectorial components of the near fields induced in the nanoresonator. Figure 5(a) shows this effect by inverting Eq. (4) for extracting the volume-averaged magnitudes of the induced near fields $\overline{|\mathbf{E_v}|^4}$ in MoS_2 nanoresonators via analysis of the anisotropic Raman modes. The values were normalized by the averaged near field $\overline{|\mathbf{E_{x,film}}|^4}$ extracted from the Raman spectrum of a thin MoS_2 flake of the same thickness, where we assumed a signal originated by

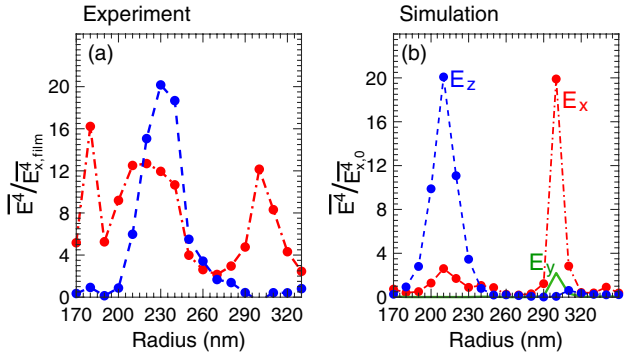

Fig. 5. Extracting the vectorial near-field enhancement from Raman measurements. (a) Variation in volume-averaged $\overline{|\mathbf{E_x}|^4}$ and $\overline{|\mathbf{E_z}|^4}$ near-field amplitudes with the nanocone bottom radius. The data is extracted from Raman data by inverting Eq. (4) and normalized by the average in-plane field extracted from the Raman signal of a thin film. (b) The corresponding simulated electric field enhancement factors $|\mathbf{E}_v/\mathbf{E}_0|^4$ ($v = x, y, z$) as functions of the nanocone bottom radius induced at the wavelength of 785 nm.

a diffraction-limited illumination area. To verify the obtained electric field magnitudes, we compared them to the electric field enhancement factors obtained from FDTD simulations of the corresponding structures illuminated at the wavelength of 785 nm [Fig. 5(b)]. Despite the approximations made in our derivation, the values extracted from the Raman measurements are in good overall agreement with the simulations. The resonances in the simulated data are shifted to slightly smaller radii compared to the experimental data, but this does not come as a surprise if one considers the differences between the experiment and FDTD simulations already observed in the elastic scattering spectra in Fig. 2. These differences highlight the needs for experimental measurements to estimate the internal fields, particularly for those structures with complicated spectral features.

5. CONCLUSION

In summary, we have investigated the effects of material anisotropy in cone-shaped single-crystal MoS_2 transition metal dichalcogenide nanoresonators using extinction measurements, inelastic scattering from Raman active phonons, and extensive electrodynamics simulations. The nanoresonators support geometrical Mie resonances in the visible to near-infrared spectral range due to their large in-plane refractive index and in spite of a much lower out-of-plane index. We showed that is possible to utilize the material anisotropy not only to modify the resonance of the nanostructures but also to probe the polarization and relative magnitudes of the enhanced near fields inside a nanoresonator using Raman scattering analysis.

Anisotropic optical responses in nanophotonics are typically associated with shape anisotropy induced through nanostructuring. TMDC materials offer an additional degree of freedom in the design of nanophotonic structures as the intrinsic material anisotropy also strongly influences far-field spectra, field enhancement, and near-field polarization. Nanostructuring and material anisotropy thus constitute an extremely powerful and flexible means for tailoring the optical response of nanophotonic systems and for exploring new avenues for research and applications.

Funding. Knut och Alice Wallenbergs Stiftelse; Vetenskapsrådet.

Acknowledgment. This work was partly conducted at Myfab Chalmers.

Disclosures. The authors declare no conflicts of interest.

See Supplement 1 for supporting content.

REFERENCES

1. A. I. Kuznetsov, A. E. Miroshnichenko, M. L. Brongersma, Y. S. Kivshar, and B. Luk'yanchuk, "Optically resonant dielectric nanostructures," Science **354**, aag2472 (2016).
2. D. Lin, P. Fan, E. Hasman, and M. L. Brongersma, "Dielectric gradient metasurface optical elements," Science **345**, 298 (2014).
3. M. I. Shalaev, J. Sun, A. Tsukernik, A. Pandey, K. Nikolskiy, and N. M. Litchinitser, "High-efficiency all-dielectric metasurfaces for ultracompact beam manipulation in transmission mode," Nano Lett. **15**, 6261–6266 (2015).
4. X. Ni, A. V. Kildishev, and V. M. Shalaev, "Metasurface holograms for visible light," Nat. Commun. **4**, 2807 (2013).
5. S. Liu, M. B. Sinclair, S. Saravi, G. A. Keeler, Y. Yang, J. Reno, G. M. Peake, F. Setzpfandt, I. Staude, T. Pertsch, and I. Brener, "Resonantly enhanced second-harmonic generation using III–V semiconductor all-dielectric metasurfaces," Nano Lett. **16**, 5426–5432 (2016).
6. G. Grinblat, Y. Li, M. P. Nielsen, R. F. Oulton, and S. A. Maier, "Efficient third harmonic generation and nonlinear subwavelength imaging at a higher-order anapole mode in a single germanium nanodisk," ACS Nano **11**, 953–960 (2017).
7. M. L. Brongersma, Y. Cui, and S. Fan, "Light management for photovoltaics using high-index nanostructures," Nat. Mater. **13**, 451–460 (2014).
8. R. Vismara, N. O. Länk, R. Verre, M. Käll, O. Isabella, and M. Zeman, "Solar harvesting based on perfect absorbing all-dielectric nanoresonators on a mirror," Opt. Express **27**, A967–A980 (2019).
9. N. Bosio, H. Šípová-Jungová, N. O. Länk, T. J. Antosiewicz, R. Verre, and M. Käll, "Plasmonic versus all-dielectric nanoantennas for refractometric sensing: a direct comparison," ACS Photon. **6**, 1556–1564 (2019).
10. O. Yavas, M. Svedendahl, P. Dobosz, V. Sanz, and R. Quidant, "On-a-chip biosensing based on all-dielectric nanoresonators," Nano Lett. **17**, 4421–4426 (2017).
11. M. Caldarola, P. Albella, E. Cortés, M. Rahmani, T. Roschuk, G. Grinblat, R. F. Oulton, A. V. Bragas, and S. A. Maier, "Non-plasmonic nanoantennas for surface enhanced spectroscopies with ultra-low heat conversion," Nat. Commun. **6**, 7915 (2015).
12. D. E. Aspnes and A. Studna, "Dielectric functions and optical parameters of Si, Ge, GaP, GaAs, GaSb, InP, InAs, and InSb from 1.5 to 6.0 eV," Phys. Rev. B **27**, 985 (1983).
13. F. Aieta, M. A. Kats, P. Genevet, and F. Capasso, "Multiwavelength achromatic metasurfaces by dispersive phase compensation," Science **347**, 1342 (2015).
14. S. Jahani, S. Kim, J. Atkinson, J. C. Wirth, F. Kalhor, A. A. Noman, W. D. Newman, P. Shekhar, K. Han, V. Van, R. G. DeCorby, L. Chrostowski, M. Qi, and Z. Jacob, "Controlling evanescent waves using silicon photonic all-dielectric metamaterials for dense integration," Nat. Commun. **9**, 1893 (2018).
15. S. Jahani and Z. Jacob, "Transparent subdiffraction optics: nanoscale light confinement without metal," Optica **1**, 96–100 (2014).
16. O. Takayama, D. Artigas, and L. Torner, "Lossless directional guiding of light in dielectric nanosheets using Dyakonov surface waves," Nat. Nanotechnol. **9**, 419–424 (2014).
17. R. Verre, N. Maccaferri, K. Fleischer, M. Svedendahl, N. Odebo Lank, A. Dmitriev, P. Vavassori, I. V. Shvets, and M. Kall, "Polarization conversion-based molecular sensing using anisotropic plasmonic metasurfaces," Nanoscale **8**, 10576–10581 (2016).
18. Y. Zhao and A. Alù, "Manipulating light polarization with ultrathin plasmonic metasurfaces," Phys. Rev. B **84**, 205428 (2011).
19. D. N. Basov, M. M. Fogler, and F. J. García de Abajo, "Polaritons in van der Waals materials," Science **354**, aag1992 (2016).
20. J. D. Caldwell, A. V. Kretinin, Y. Chen, V. Giannini, M. M. Fogler, Y. Francescato, C. T. Ellis, J. G. Tischler, C. R. Woods, A. J. Giles, M. Hong, K. Watanabe, T. Taniguchi, S. A. Maier, and K. S. Novoselov, "Sub-diffractional volume-confined polaritons in the natural hyperbolic material hexagonal boron nitride," Nat. Commun. **5**, 5221 (2014).
21. Q. H. Wang, K. Kalantar-Zadeh, A. Kis, J. N. Coleman, and M. S. Strano, "Electronics and optoelectronics of two-dimensional transition metal dichalcogenides," Nat. Nanotechnol. **7**, 699 (2012).
22. A. Kuc, N. Zibouche, and T. Heine, "Influence of quantum confinement on the electronic structure of the transition metal sulfide TS2," Phys. Rev. B **83**, 245213 (2011).
23. H. Zhang, J. Choi, A. Ramani, D. Voiry, S. N. Natoli, M. Chhowalla, D. R. McMillin, and J. H. Choi, "Engineering chemically exfoliated large-area two-dimensional MoS2 nanolayers with porphyrins for improved light harvesting," ChemPhysChem **17**, 2854–2862 (2016).
24. O. Lopez-Sanchez, E. A. Llado, V. Koman, A. Fontcuberta i Morral, A. Radenovic, and A. Kis, "Light generation and harvesting in a van der Waals heterostructure," ACS Nano **8**, 3042–3048 (2014).
25. B. Peng, P. K. Ang, and K. P. Loh, "Two-dimensional dichalcogenides for light-harvesting applications," Nano Today **10**(2), 128–137 (2015).
26. M.-L. Tsai, S.-H. Su, J.-K. Chang, D.-S. Tsai, C.-H. Chen, C.-I. Wu, L.-J. Li, L.-J. Chen, and J.-H. He, "Monolayer MoS2 heterojunction solar cells," ACS Nano **8**, 8317–8322 (2014).
27. T. F. Jaramillo, K. P. Jørgensen, J. Bonde, J. H. Nielsen, S. Horch, and I. Chorkendorff, "Identification of active edge sites for electrochemical H2 evolution from MoS2 nanocatalysts," Science **317**, 100 (2007).

28. D. A. Henckel, O. M. Lenz, K. M. Krishnan, and B. M. Cossairt, "Improved HER catalysis through facile, aqueous electrochemical activation of nanoscale WSe2," Nano Lett. **18**, 2329–2335 (2018).
29. M. Asadi, K. Kim, C. Liu, A. V. Addepalli, P. Abbasi, P. Yasaei, P. Phillips, A. Behranginia, J. M. Cerrato, R. Haasch, P. Zapol, B. Kumar, R. F. Klie, J. Abiade, L. A. Curtiss, and A. Salehi-Khojin, "Nanostructured transition metal dichalcogenide electrocatalysts for CO2 reduction in ionic liquid," Science **353**, 467 (2016).
30. Y. Wang, L.-T. Tseng, P. P. Murmu, N. Bao, J. Kennedy, M. Ionesc, J. Ding, K. Suzuki, S. Li, and J. Yi, "Defects engineering induced room temperature ferromagnetism in transition metal doped MoS2," Mater. Design **121**, 77–84 (2017).
31. K. Premasiri and X. P. A. Gao, "Tuning spin–orbit coupling in 2D materials for spintronics: a topical review," J. Phys. Condens. Matter **31**, 193001 (2019).
32. J. Wen, H. Wang, W. Wang, Z. Deng, C. Zhuang, Y. Zhang, F. Liu, J. She, J. Chen, H. Chen, S. Deng, and N. Xu, "Room-temperature strong light–matter interaction with active control in single plasmonic nanorod coupled with two-dimensional atomic crystals," Nano Lett. **17**, 4689–4697 (2017).
33. J. Cuadra, D. G. Baranov, M. Wersäll, R. Verre, T. J. Antosiewicz, and T. Shegai, "Observation of tunable charged exciton polaritons in hybrid monolayer WS2–plasmonic nanoantenna system," Nano Lett. **18**, 1777–1785 (2018).
34. R. Verre, D. G. Baranov, B. Munkhbat, J. Cuadra, M. Käll, and T. Shegai, "Transition metal dichalcogenide nanodisks as high-index dielectric Mie nanoresonators," Nat. Nanotechnol. **14**, 679–683 (2019).
35. A. R. Beal and H. P. Hughes, "Kramers-Kronig analysis of the reflectivity spectra of 2H-MoS2, 2H-MoSe2and 2H-MoTe2," J. Phys. C **12**, 881–890 (1979).
36. R. F. Frindt, A. D. Yoffe, and F. P. Bowden, "Physical properties of layer structures: optical properties and photoconductivity of thin crystals of molybdenum disulphide," Proc. R. Soc. London Ser. A **273**, 69–83 (1963).
37. R. Bailly, "Infrared light for mineral determination," Am. Mineral. **33**, 519 (1948).
38. R. A. Neville and B. L. Evans, "The band edge excitons in 2H-MoS2," Phys. Status Solidi **73**, 597 (1976).
39. D. Hu, X. Yang, C. Li, R. Liu, Z. Yao, H. Hu, S. N. G. Corder, J. Chen, Z. Sun, M. Liu, and Q. Dai, "Probing optical anisotropy of nanometer-thin van der waals microcrystals by near-field imaging," Nat. Commun. **8**, 1471 (2017).
40. M. Kerker, D. S. Wang, and C. L. Giles, "Electromagnetic scattering by magnetic spheres," J. Opt. Soc. Am. **73**, 765–767 (1983).
41. Y. H. Fu, A. I. Kuznetsov, A. E. Miroshnichenko, Y. F. Yu, and B. Luk'yanchuk, "Directional visible light scattering by silicon nanoparticles," Nat. Commun. **4**, 1527 (2013).
42. S. Person, M. Jain, Z. Lapin, J. J. Sáenz, G. Wicks, and L. Novotny, "Demonstration of zero optical backscattering from single nanoparticles," Nano Lett. **13**, 1806–1809 (2013).
43. N. Papasimakis, V. A. Fedotov, V. Savinov, T. A. Raybould, and N. I. Zheludev, "Electromagnetic toroidal excitations in matter and free space," Nat. Mater. **15**, 263 (2016).
44. R. Regmi, J. Berthelot, P. M. Winkler, M. Mivelle, J. Proust, F. Bedu, I. Ozerov, T. Begou, J. Lumeau, H. Rigneault, M. F. García-Parajó, S. Bidault, J. Wenger, and N. Bonod, "All-dielectric silicon nanogap antennas to enhance the fluorescence of single molecules," Nano Lett. **16**, 5143–5151 (2016).
45. D. G. Baranov, R. Verre, P. Karpinski, and M. Käll, "Anapole-enhanced intrinsic Raman scattering from silicon nanodisks," ACS Photon. **5**, 2730–2736 (2018).
46. P. Yu and M. Cardona, *Fundamentals of Semiconductors* (Springer, 2010).
47. R. Loudon, "The Raman effect in crystals," Adv. Phys. **50**, 813–864 (2001).
48. P. A. Dmitriev, D. G. Baranov, V. A. Milichko, S. V. Makarov, I. S. Mukhin, A. K. Samusev, A. E. Krasnok, P. A. Belov, and Y. S. Kivshar, "Resonant Raman scattering from silicon nanoparticles enhanced by magnetic response," Nanoscale **8**, 9721–9726 (2016).
49. E. C. Le Ru and P. G. Etchegoin, "Rigorous justification of the |E|4 enhancement factor in surface enhanced Raman spectroscopy," Chem. Phys. Lett. **423**, 63–66 (2006).